Dalton Transactions

ROYAL SOCIETY OF CHEMISTRY

PAPER

View Article Online
View Journal | View Issue

Cite this: *Dalton Trans.*, 2026, **55**, 5336

Experimental and theoretical insights into the incorporation of MACl in $FAPbI_3$ perovskite films

Nazlıcan Şahin Sütcü, *[a] Pelin Kavak,[b] Ayşenur Corcor Özbay,[a] İrem Topal,[c] Neşe Güngör,[a] Emrah Çakmakçı,[c] Kadir Esmer,[a] Caner Değer,[a] İlhan Yavuz[a] and Mustafa Alevli*[a]

In this study, we investigate how methylammonium chloride (MACl) affects the formation and optoelectronic properties of $FAPbI_3$ perovskite films. The perovskite precursor molarity was systematically varied (1.46–1.80 M) while keeping the MACl additive level constant at 20 mol% with respect to $FAPbI_3$, and a chloride-rich condition (1.2 M with 50 mol% MACl) was additionally examined. Using SEM, XRD, FTIR, and steady-state/time-resolved photoluminescence together with density functional theory (DFT), we establish a direct correlation between MACl-driven crystallization, facet-selective growth, and the resulting structural and optoelectronic properties. XRD reveals enhanced α-phase purity and strengthened (001) preferential orientation upon MACl addition, without any significant or systematic peak shift beyond minor lattice variations. EDS confirms residual chlorine retention after annealing. DFT rationalizes these findings through a dual-ion compensation mechanism, in which MA^+-induced lattice contraction and Cl^--induced expansion nearly cancel, preserving the lattice framework while stabilizing the α-$FAPbI_3$ phase. These results provide mechanistic insight into MACl-assisted stabilization and clarify the structural origin of performance improvements in FA-based perovskite solar cells.

Received 24th December 2025,
Accepted 11th March 2026

DOI: 10.1039/d5dt03070f

rsc.li/dalton

Introduction

Formamidinium-based lead triiodide ($FAPbI_3$) has become an important research topic in the field of perovskite solar cells in recent years. Due to its high efficiency potential and cost-effective advantages, $FAPbI_3$ has attracted great interest compared to conventional solar cells. This perovskite structure has two main crystalline phases: yellow phase (δ) and black phase (α). The black α phase stands out as an ideal material for the development of high-efficiency solar cells due to its wide bandgap. However, the α phase of $FAPbI_3$ is unstable due to the large size of the FA^+ cation and often tends to transform into the yellow phase. This phase transformation can adversely affect the performance of solar cells. Therefore, various dopants, such as methylammonium, cesium and bromine, are used to improve the stability of the α phase. These dopants not only inhibit phase transformation, but also have the potential to improve the electrical properties of perovskite films by broadening the bandgap.[1,2] It has been observed that the efficiency of perovskite solar cells (PSC) obtained by using various additives increases with the widening of the bandgap. These additives not only increase the stability of the perovskite structure but also improve the photovoltaic performance. In particular, decreasing defect density and increasing activation energy greatly improved the efficiency of PSCs.[3] Min *et al.* showed that doping the α-$FAPbI_3$ phase with methylenediammonium dichloride (DMAI) yielded a power conversion efficiency of 23.7%, which was maintained after 600 h of operation. These findings reveal the potential of DMAI to increase the stability and improve the performance of the perovskite structure.[4] Similarly, DMAI has been reported to be an effective volatile additive for manipulating the crystallisation process of inorganic perovskite films.[5] In the studies, it was observed that the addition of methylammonium chloride (MACl) to $FAPbI_3$ significantly increased the particle size and crystallinity of the perovskite film. This indicated that MACl acts as a 'transition stabiliser' and provides a positive effect that improves the efficiency of $FAPbI_3$ cells.[6–8] In another study in 2023, alkylammonium chlorides (RACl) were added to the $FAPbI_3$ structure and the certified power efficiency was reported as 25.7%.[9] The addition of MACl has been reported to significantly improve the crystallinity of the perovskite and the efficiency of the devices, but excessive or insufficient addition has been found to lead to defects and performance loss.[10] The mechanism of action of MACl, which positively affects the performance in perovskite solar cells, is still not

[a]*Physics Department, Marmara University, Istanbul, 34722, Turkey.*
E-mail: mustafaalevli@marmara.edu.tr, nazlican.sahin@marmara.edu.tr
[b]*Department of Physics, Faculty of Arts and Sciences, Yıldız Technical University, 34220 Istanbul, Turkey*
[c]*Chemistry Department, Marmara University, Istanbul, 34722, Turkey*

clearly known. Studies to date have used the incorporation of methylammonium chloride (MACl), which leads to films with improved properties such as high crystallinity and preferential orientation. However, previous studies have detected undesirable residual methylammonium in the resulting PSCs.[11] These thermally unstable organic species raise significant concerns about the long-term operational stability of the devices, even when the amount of methylammonium included is relatively small.[12] Kang *et al.* investigates the effect of residual chloride from MACl on the $FAPbI_3$ perovskite films. They found that residual chloride remains in the perovskite film and propose a solution through post-heat treatment (PHT) to remove chloride ions.[13]

In this study, we explore MACl-assisted $FAPbI_3$ film formation using two complementary conditions. Unlike previous reports that primarily focus on the presence or absence of MACl, this work decouples precursor molarity effects from additive loading, enabling a systematic correlation between structural stabilization and device optimization. First, we vary the $FAPbI_3$ precursor molarity (1.46, 1.63, and 1.8 M) at a fixed MACl loading of 20 mol% (relative to $FAPbI_3$) to isolate precursor-concentration effects on crystallization, morphology, and device performance. Second, we include a low-molarity, high-MACl formulation (1.2 M with 50 mol% MACl) as a chloride-rich reference to assess how increased additive content further influences phase stability and film quality. Based on the proposed compensating roles of MA^+ and Cl^- in the lattice, we examine whether any measurable lattice response accompanies MACl processing using XRD and EDS. Experimental characterization is complemented by DFT calculations to elucidate the structural origin of these trends.

Experimental section

Materials

In this study, chlorobenzene (99.8%, Sigma-Aldrich), formamidinium iodide (FAI) (≥98%,), *N*,*N*-dimethylformamide (99.8%), dimethyl sulfoxide (99.9%), spiro-OMeTAD (%99), 4-tertbutylpyridine (98%), and lithium bis(trifluoromethylsulphonyl) imide (99.95%) were purchased from Sigma Aldrich. PbI_2 (99.99%), and methylamine hydrochloride (MACl, ≥98%) was procured from TCI. The following materials were also used [6,6]-Phenyl C61 butyric acid methyl ester (PC61BM) (LUMTEC), PEDOT:PSS (Heraeus Clevios GmbH), fluorine doped tin oxide (FTO) coated glass substrates (NSG, TEC 15) and indium tin oxide (ITO(KINTEC,TEC 10)). Tin(IV) oxide, 15% in H_2O colloidal dispersion was supplied from Alfa Aesar. Silver pellets were purchased from Kurt J. Lesker Company.

Device fabrication

To investigate the effect of MACl on the performance of $FAPbI_3$-based devices, we fabricated PSC devices using four precursor formulations. The device structure is configured as FTO/SnO_2/perovskite/Spiro-OMeTAD/V_2O_5/Ag, as illustrated in Fig. 1.

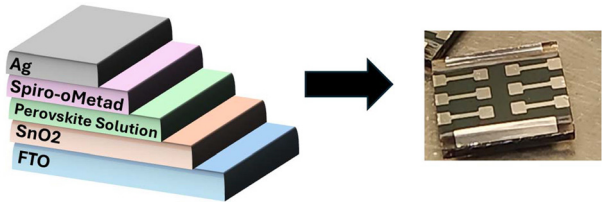

Fig. 1 The device structure of pristine and MACl-treated $FAPbI_3$ (FTO/SnO_2/perovskite/Spiro-OMeTAD/V_2O_5/Ag).

The $FAPbI_3$ solution was prepared by dissolving 43 mg formamidinium iodide (FAI) and 116 mg PbI_2 powders in a dimethylformamide (DMF)/dimethyl sulfoxide (DMSO) mixed solvent (8 : 1, v/v).[14,15] MACl/$FAPbI_3$ precursor solutions were prepared at four different perovskite molarities of 1.2 M, 1.46 M, 1.63 M and 1.8 M. For the 1.46 M, 1.63 M and 1.8 M formulations, MACl was added at 20 mol% with respect to $FAPbI_3$, whereas the 1.2 M formulation was prepared with a higher MACl loading of 50 mol% (chloride-rich condition). The 1.2 M MACl-added $FAPbI_3$ solution was prepared by dissolving 51.5 mg of FAI, 138.5 mg of PbI_2 and 9.8 mg MACl in a mixed solvent of DMF/DMSO (4 : 1, v/v). The final solution was stirred at ambient temperature for 2 h. All other solutions were prepared by stirring at room temperature for 30 min. The perovskite solutions with and without MACl powder were spin coated. The perovskite growth process was carried out in a single-step spin coating program at 1000 rpm for 10 s and 4000 rpm for 20 s. 200 μL of chlorobenzene was injected onto the film surface at 10 s prior to the end of the spinning process. After coating, the perovskite films, with and without MACl, were annealed at 150 °C for 15 min to complete the perovskite phase. The substrates were cooled down for few minutes and 50 μL Spiro-OMeTAD solution doped with lithium bis(trifluoromethanesulfonyl)imide (Li-TFSI) and 4-*tert*-butyl pyridine was spin coated dynamically on a rotating substrate at 4000 rpm for 30 s. The hole transport material solution (chlorobenzene as the solvent) was prepared by dissolving 72.3 mg spiro-OMeTAD, 28.8 μL 4-*tert*-butylpyridine, and 17.5 μL Li-TFSI (520 mg mL^{-1} in acetonitrile). Finally, approximately 10 nm of V_2O_5 and 100 nm of Ag were thermally evaporated as the counter electrode onto the hole transport layer under a vacuum of about 10^{-6} Pa, forming the back contact. The PSCs have an active area of 0.09 cm^2.

Film characterization

Surface and cross-sectional views were examined using a scanning electron microscope (SEM, THERMOSCIENTIFIC, QUATTRO S SEM). Cross-sectional SEM samples were prepared by mechanical cutting of the device using a diamond cutter. The crystal structure of the perovskite samples was determined by X-ray diffraction (XRD) experiment. The XRD pattern of the samples was obtained by a Shimadzu XRD-7000 (40 kV, 30 mA) under monochromated Cu-Kα radiation and the scan rate of 2° per min. Steady-state PL spectra were obtained using an Edinburgh Instruments FS5 spectrometer equipped with a

405 nm pulsed laser. Ultraviolet–visible (UV-Vis) spectra of perovskite films were obtained with PerkinElmer Lambda 35 UV/Vis spectrometer. Spectra were analyzed between 200 nm and 1100 nm wavelengths. The Fourier Transform Infrared Spectroscopy (FTIR) measurements were performed in the attenuated total reflection (ATR) mode in the 4000–400 cm^{-1} range. FTIR employing a PerkinElmer ATR-FTIR Spectrometer was used for the measurements and performed in transmittance mode. Surface morphology of the films was investigated with AFM Workshop TT model atomic force microscope (AFM). AFM measurements were performed in vibration mode using silicon tips. The scan rate was 0.5 Hz.

Device characterization

The current density–voltage (*J–V*) curves were recorded using a Keithley 2420-C digital source meter under AM 1.5G illumination conditions (100 mW cm^{-2}) provided by a LOT solar simulator equipped with a 500 W Xenon lamp. The solar simulator was calibrated using a reference silicon solar cell to ensure accuracy. Measurements were taken at a scan rate of 0.1 V s^{-1}, covering a voltage range from 1.2 V to −0.1 V and *vice versa*, with increments of 0.005 V. All solar cell measurements were performed under ambient conditions within a nitrogen-filled glove box to maintain optimal conditions and prevent moisture exposure.

Computer analysis

Density Functional Theory (DFT) calculations were carried out using the Vienna *Ab initio* Simulation Package (VASP). All geometry optimizations and self-consistent field calculations utilized the Perdew–Burke–Ernzerhof (PBE) exchange–correlation functional within the generalized gradient approximation (GGA). Projector-Augmented-Wave (PAW) pseudopotentials were used to model the interactions between core and valence electrons.[16–18] For the bulk $FAPbI_3$ structure, a 2 × 2 × 2 supercell was utilized with corresponding gamma-centered k-points set to 2 × 2 × 2, allowing full relaxation of ions and cell parameters (ISIF = 3). For the surface studies, a 2 × 2 × 1 supercell with a 2 × 2 × 1 *k*-point mesh was used, and a slab approximately 10^{-15} Å thick was constructed along the [001] direction, with only the ionic positions relaxed (ISIF = 2). Both configurations incorporated MACl in varying alignments. All computations ensured that the forces on atoms and ions were minimized to below 0.01 eV $Å^{-1}$, to accurately reflect the optimized geometry. The electronic wave functions were described using plane waves with an energy cutoff of 400 eV. This setup provided a comprehensive understanding of the structural and electronic properties of both bulk and surface modified $FAPbI_3$ doped with MACl.

To predict the formation energies, the following formula was utilized:

$$\Delta H_f = E_f - E_0 + \sum_i \Delta n_i \mu_i$$

Here, E_f represents the energy of the supercell with MACl incorporated, and E_0 is the energy of the pristine supercell. μ_i is the chemical potential of the incorporated or removed species, and Δn_i indicates the number of atoms added or removed to generate the modified structure. This method quantifies the energy change due to the incorporation of MACl in $FAPbI_3$ structures, highlighting the thermodynamic stability of the doped configurations.

Results and discussion

The surface morphologies of the film compositions with varying molarity and MACl content were investigated using SEM images. The grain size of the perovskite film was observed to correlate directly with the MACl content.

Fig. 2A–D compares MACl-treated films, where the 1.46–1.80 M series contains the same MACl loading (20 mol%)

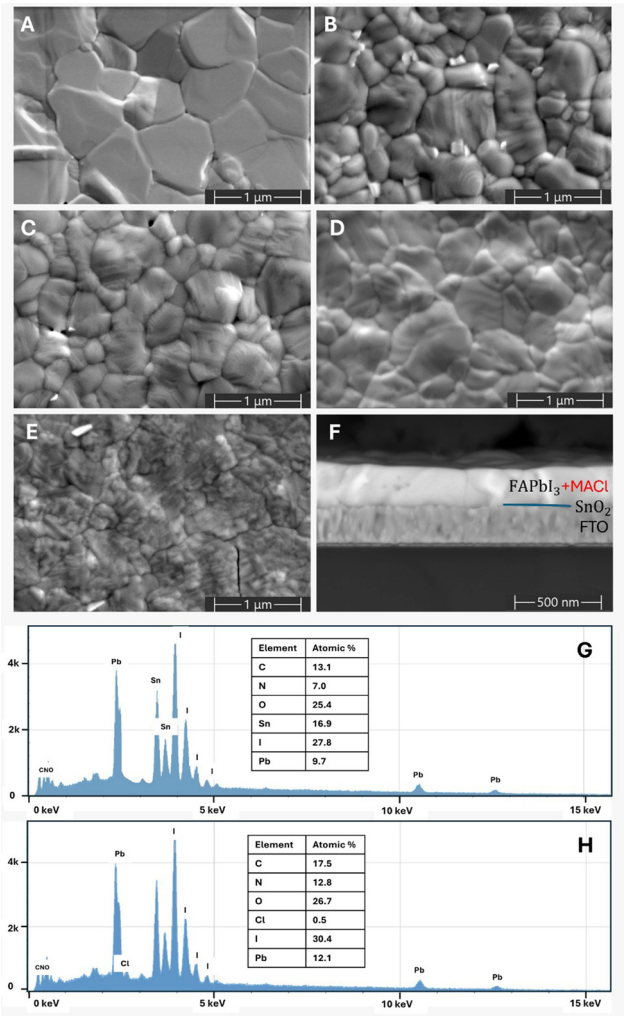

Fig. 2 SEM images of perovskite films: (A) 1.2 M (50 mol% MACl), (B) 1.46 M (20 mol% MACl), (C) 1.63 M (20 mol% MACl), (D) 1.8 M (20 mol% MACl), (E) pristine $FAPbI_3$ (no MACl), and (F) cross-sectional SEM image of the 1.63 M MACl-treated $FAPbI_3$ perovskite film, (G) EDS spectrum of pristine $FAPbI_3$ (no MACl), and (H) EDS spectrum of 1.63 M (20 mol% MACl) $FAPbI_3$ perovskite film.

and the 1.2 M film contains a higher MACl loading (50 mol%) as a chloride-rich reference. The grain size and surface coverage depend on both precursor molarity and MACl loading. Notably, the 1.2 M (50 mol% MACl) film shows the largest grains (~2.6 μm) and a more homogeneous surface. Within the constant-MACl series (20 mol%), the average grain sizes are ~1.45 μm (1.46 M), ~1.61 μm (1.63 M), and ~2.08 μm (1.8 M), indicating that precursor concentration also influences crystallization. The cross-sectional SEM image (Fig. 2F) confirms well-defined FTO/SnO_2/perovskite layering with distinct interfaces and no obvious void formation.

Fig. 2G and H show the EDS spectra of pristine $FAPbI_3$ and 1.63 M MACl-doped $FAPbI_3$ perovskite films, respectively. EDS analysis confirmed the absence of Cl in the pristine $FAPbI_3$. In the perovskite film doped with MACl, a Cl signal (~0.5%) was observed. This indicates that Cl was not completely removed during annealing and was partially retained within the structure.

Fig. 3 shows the X-ray diffraction (XRD) patterns of the perovskite films. The addition of MACl improves the crystallinity and phase purity of $FAPbI_3$. In particular, the δ-phase impurity peak is suppressed upon MACl incorporation, while the preferred orientation peaks at 14.19° (001) and 28.33° (002) become more intense.[19,20]

Among the investigated conditions, the 1.2 M film (prepared with higher MACl loading, 50 mol%) exhibits the highest α-phase purity and the strongest preferential orientation along the [001] direction.

Although minor variations are observed, the XRD peak positions do not show a systematic shift beyond instrumental resolution, consistent with DFT results showing compensating effects of MA^+ (volume contraction) and Cl^- (volume expansion) that nearly cancel when both ions are present, leading to negligible net lattice change (Fig. 8E). As shown in Fig. 2, the increase in the preferred orientation correlated with the increase in particle size and morphological order. Furthermore, the calculated *d*-spacing changes from 6.23 Å (pristine $FAPbI_3$) to a maximum of 6.33 Å for the MACl-containing samples, corresponding to a variation of less than 2%. These small variations are consistent with microstrain and compensating lattice effects of MA^+ and Cl^- incorporation rather than a structural phase change. Thus, the crystal structure is essentially preserved despite minor lattice adjustments.

The most intense diffraction features belong to the (001) plane family, emphasizing preferential growth along the [001] direction. Furthermore, the diffraction intensity of the (001) facet increased by approximately 1500% with higher MACl content. This suggests that MACl selectively reduces the surface energy of this facet and promotes its growth.

As a result, the chloride-rich composition (1.2 M) delays the δ-to-α phase transformation, leading to larger grains and improved crystal alignment, as also observed in Fig. 2.[21] In contrast, the (011) facet shows no further increase in intensity, highlighting the facet-selective nature of MACl-induced stabilization. Overall, these results indicate that MACl incorporation not only suppresses secondary phases but also directs prefer-

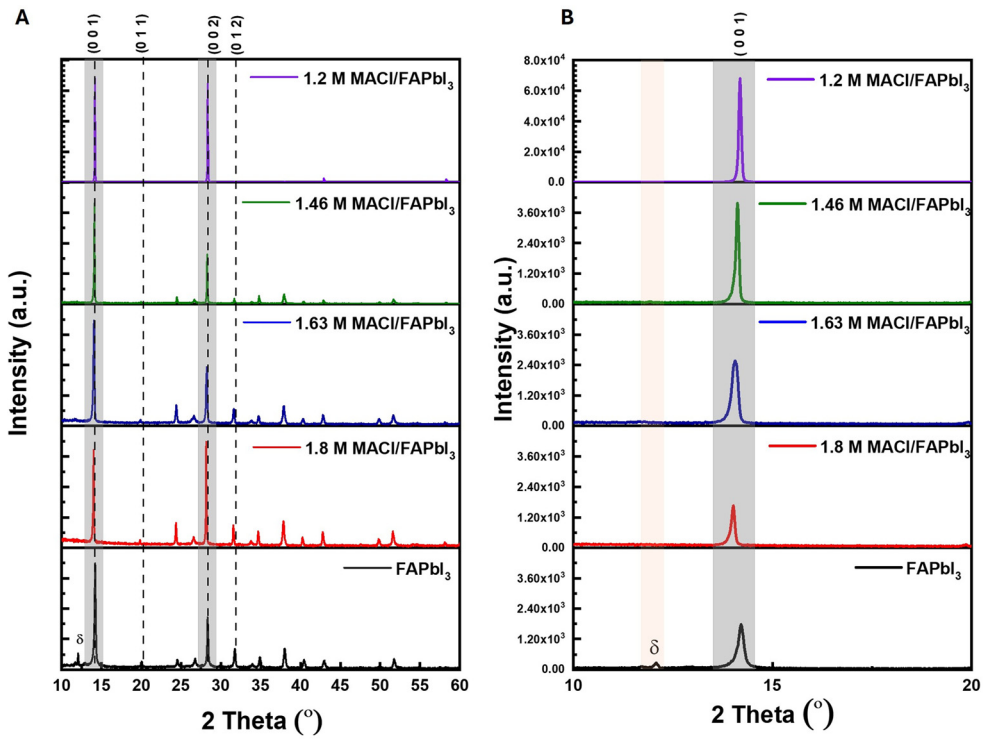

Fig. 3 XRD patterns of MACl-doped and undoped perovskite films. (A) Appearance of the 2-Theta angle in the range of 5° to 60°. (B) Appearance of the crystal plane (0 0 1) of the α-$FAPbI_3$ phase in the range of 10° to 20°.

ential growth, thereby optimizing the crystallization pathway of $FAPbI_3$ films.

To analyze the surface topography of perovskite films prepared at different MACl contents, AFM measurements were performed and roughness values were extracted for each sample. AFM images at a scale of 15 μm × 15 μm were shown in Fig. 4A–E for pristine and MACl-treated $FAPbI_3$. Film roughness was evaluated using the root mean square (RMS) roughness. The surface roughness was measured as 64.19 nm, 39.88 nm, 32.52 nm, 29.15 nm and 26.42 nm for 1.2 M (50 mol% MACl), 1.46 M (20 mol% MACl), 1.63 M (20 mol% MACl), 1.8 M(20 mol% MACl), and $FAPbI_3$, respectively. 1.2 M (chloride rich) film shows a laterally more uniform and homogeneous coverage, yet a relatively high RMS value. This can arise because RMS roughness is highly sensitive to long-range topography and peak-to-valley height variations; the presence of larger, preferentially oriented grains can increase the height amplitude within the scan area, resulting in a higher RMS even when surface coverage is uniform. Therefore, the higher RMS in the 1.2 M film does not necessarily indicate poorer film quality, but rather reflects pronounced vertically developed features associated with oriented crystal growth. Overall, these results indicate that MACl loading and precursor conditions modify the surface texture of the perovskite films, consistent with the SEM and XRD trends (Fig. 2 and 3).

Fig. 5 presents the FTIR spectra of the perovskite films, highlighting changes induced by MACl addition. The peaks at 1710, 1353, 1048 and 590 cm^{-1} become more pronounced upon MACl treatment of $FAPbI_3$ and can be assigned to C═N stretching, C–H bending, N–H rocking and C–H rocking vibrations, respectively.[21] The C═N stretching at ~1710 cm^{-1} and the N–H rocking/C–H bending features around ~1048 and ~1353 cm^{-1} are characteristic of the FA^+-containing lattice, whereas the C–N stretching region between 960–1000 cm^{-1} remains largely unchanged, suggesting that MACl does not strongly perturb this particular vibrational mode. In addition, the broad N–H stretching band in the ~3300–3500 cm^{-1} range is consistent with MA^+/FA^+-containing films.[22] During perovskite crystallization/annealing, a minor fraction of volatile organic iodide species (*e.g.*, FAI-related components) can be lost, while the persistence of FA^+-related bands indicates that the major fraction remains in the final film. Overall, the FTIR spectra indicate that MACl modifies the vibrational signatures of the organic sublattice without drastically altering the bonding environment of the FA^+ cation. Because FTIR does not directly identify Cl^-, the presence and impact of MA^+ and Cl^- incorporation into the perovskite lattice are addressed later by DFT calculations.

To evaluate the effect of MACl and perovskite molar concentration on the interfacial charge transfer kinetics, we measured the photoluminescence (PL) spectra of $FAPbI_3$ films on FTO/SnO_2 substrates. Fig. 6A shows the room-temperature steady-state PL spectra of the perovskite films. The PL peaks are centered around ~823 nm, ~821 nm, ~818 nm, and ~817 nm for samples 1.2 M, 1.46 M, 1.63 M, and 1.8 M, respectively, which align with the onset values observed in the absorption spectra. Notably, the emission peak of the $FAPbI_3$-MACl-based films shifts similarly compared to the band edge data obtained from the absorption results, which are 1.513, 1.522, 1.511 and 1.521 eV for 1.2 M, 1.46 M, 1.63 M, and 1.8 M, respectively. The difference between the absorption edge and the PL peak energy indicates the Stokes shift.[23]

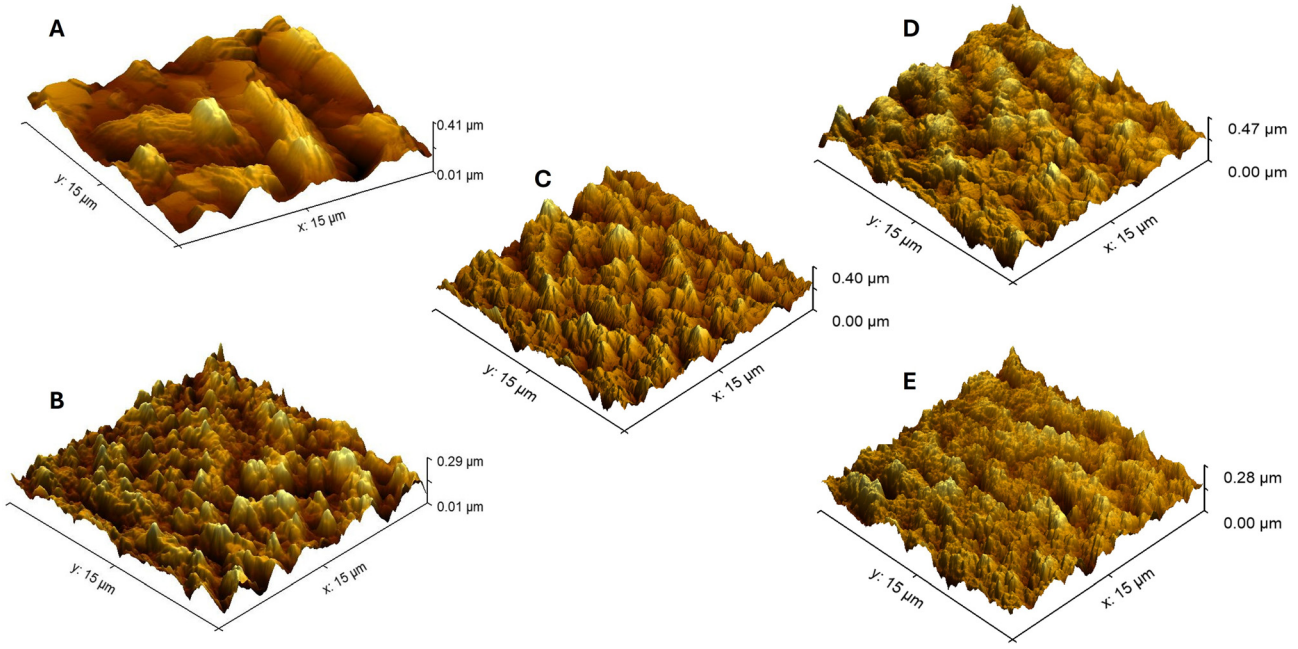

Fig. 4 AFM images of the perovskite films: (A) 1.2 M (50 mol% MACl), (B) 1.46 M(20 mol% MACl), (C) 1.63 M(20 mol% MACl), (D) 1.8 M(20 mol% MACl), and (E) $FAPbI_3$, respectively.

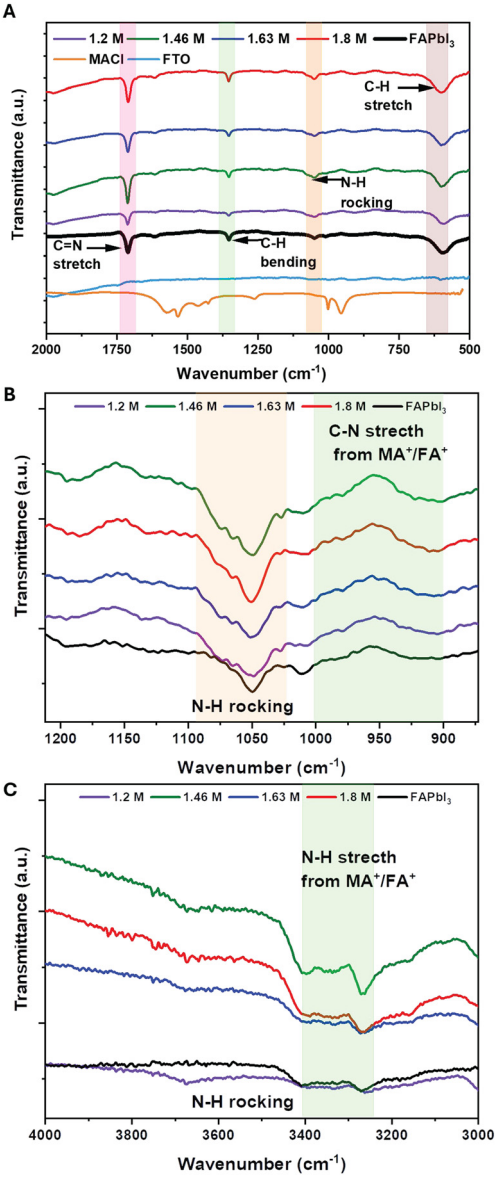

Fig. 5 The FTIR spectra of undoped and MACl-doped films. (A) Wide-range spectra (2000–500 cm^{-1}) showing characteristic vibration modes. (B) Magnified view of the fingerprint region (1225–875 cm^{-1}) highlighting the N–H rocking and C–N stretch modes originating from the MA^+/FA^+ cations. (C) N–H stretching region (4000–3000 cm^{-1}) for different molar concentrations compared to pristine $FAPbI_3$.

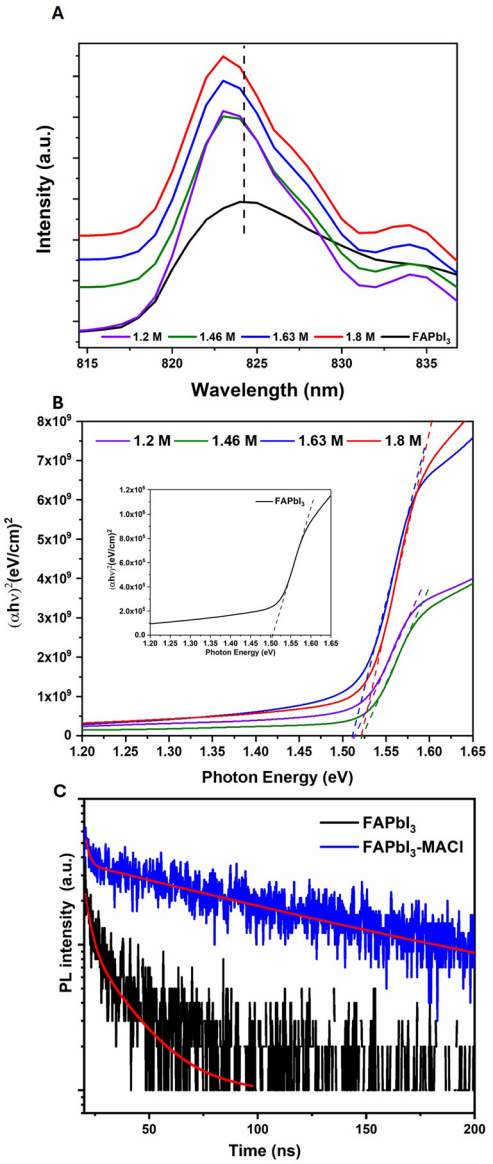

Fig. 6 (A) PL and (B) absorption spectra of $FAPbI_3$ films prepared with different concentrations (C) time-resolved PL decay at room temperature for pristine $FAPbI_3$ and 1.63 M MACl-treated $FAPbI_3$.

The Stokes shift for the 1.2 M, 1.63 M, and 1.8 M films is minimal, consistent with reduced defect-assisted relaxation processes and a high level of radiative recombination. The smallest Stokes shift observed for the 1.63 M film is consistent with reduced non-radiative losses and enhanced device performance. Fig. 6C illustrates the decay profiles of pristine $FAPbI_3$ and optimized MACl-treated film (1.63 M) at room temperature. The pristine $FAPbI_3$ film exhibits a short decay time that can be fitted with a mono-exponential function, yielding a lifetime of 106.9 ns. The mono-exponential fit (shown in red) suggests that the carriers recombine quickly, indicating the presence of non-radiative recombination centers, which can limit the overall performance of the material in solar cells. The lifetime extracted for the $FAPbI_3$-MACl film is 109 ns.

In general, longer carrier lifetimes can facilitate carrier diffusion and extraction by suppressing non-radiative recombination losses. However, the nearly identical lifetimes observed here (106.9 ns *vs.* 109 ns) indicate that MACl does not significantly alter the intrinsic recombination dynamics; therefore, the efficiency enhancement is primarily attributed to improved crystallinity/phase purity and more favorable charge-transport pathways rather than lifetime extension. The comparable TRPL lifetimes (106.9 ns *vs.* 109 ns) suggest that MACl does not markedly change the intrinsic recombination dynamics; there-

fore, the device-performance differences discussed below primarily reflect improvements in crystallinity/phase purity and charge-transport pathways.

Fig. 7(A–D) presents the statistical distributions of the key photovoltaic parameters (V_{oc}, J_{sc}, FF, and PCE) for $FAPbI_3$ (no MACl) and MACl-treated $FAPbI_3$ perovskite solar cells fabricated from different precursor formulations. V_{oc} and J_{sc} showed better values in MACl-treated solar cells compared to the pristine film. For the constant-MACl series (20 mol% MACl at 1.46–1.8 M), V_{oc} remains nearly unchanged with molarity, suggesting that band-edge energetics are not strongly affected. In contrast, J_{sc} increases with molarity and saturates at 1.63–1.8 M, consistent with the higher optical absorption observed in these films. The chloride-rich 1.2 M (50 mol% MACl) condition exhibits the highest FF, consistent with the improved phase purity and preferential orientation seen in XRD. As noted above, improved preferential orientation reduces recombination at grain boundaries and enhances carrier extraction efficiency, contributing to improved FF through reduced resistive losses. When all parameters are considered together, the overall device performance is maximized at 1.63 M (20 mol% MACl), which delivers the highest average PCE of 14.02%.

Fig. 7E shows the *J–V* curves of pristine $FAPbI_3$ perovskite solar cells, while Fig. 7F–G shows the *J–V* curves of the best performing MACl-treated $FAPbI_3$ perovskite solar cells with precursor molarities of 1.63 M and 1.46 M. The *J–V* curves show the forward and backward scan results and reveal the typical behavior of high-efficiency perovskite solar cells. For pristine $FAPbI_3$, forward scanning yields a PCE value of 8.40%, while backward scanning shows a slightly higher value of 8.55%. In perovskite solar cells with MACl addition, for a 1.63 M film, forward scanning gives a PCE value of 16.57%, while backward scanning shows a slightly higher value of 16.86%. Similarly, the 1.46 M film gives values of 14.97% (forward) and 15.74% (backward). Higher PCEs were obtained in perovskite solar cells with MACl addition. Furthermore, these results show minimal hysteresis between forward and backward scanning, reflecting stable charge transport and efficient charge collection.

Additionally, the stability test shown in Fig. 7H reveals that MACl-treated films maintain their structural integrity more effectively over time compared to pristine films. The PCE of the $FAPbI_3$ film was initially 8.40%, decreasing to 1.76% after 180 minutes. In contrast, the PCE of the MACl- treated $FAPbI_3$ film was initially measured at 11.44%. Even after 528 hours, it was measured at 10.20%, representing only a 10% loss.

To reconcile the structural findings from Fig. 3 with the photovoltaic performance trends in Fig. 7A–D, a combined interpretation is necessary. From these results, a clear distinction emerges between structural and device optimizations: the chloride-rich condition (1.2 M with 50 mol% MACl) yields the highest α-phase purity, whereas the optimized device performance is achieved at 1.63 M with a fixed MACl loading (20 mol%). In the 1.63 M film, the (001) peak intensity remains dominant and well-defined, although slightly reduced compared to chloride-rich condition, confirming that the α-phase framework is preserved.

Mechanistically, the higher MACl loading at 1.2 M more effectively suppresses the δ-phase and stabilizes the α-phase, producing structurally pure films with high FF. At slightly higher molarities (1.63 M), the optimized precursor concentration leads to higher absorption intensity in the UV-Vis spectra (Fig. 6B) and improved charge-carrier collection, result-

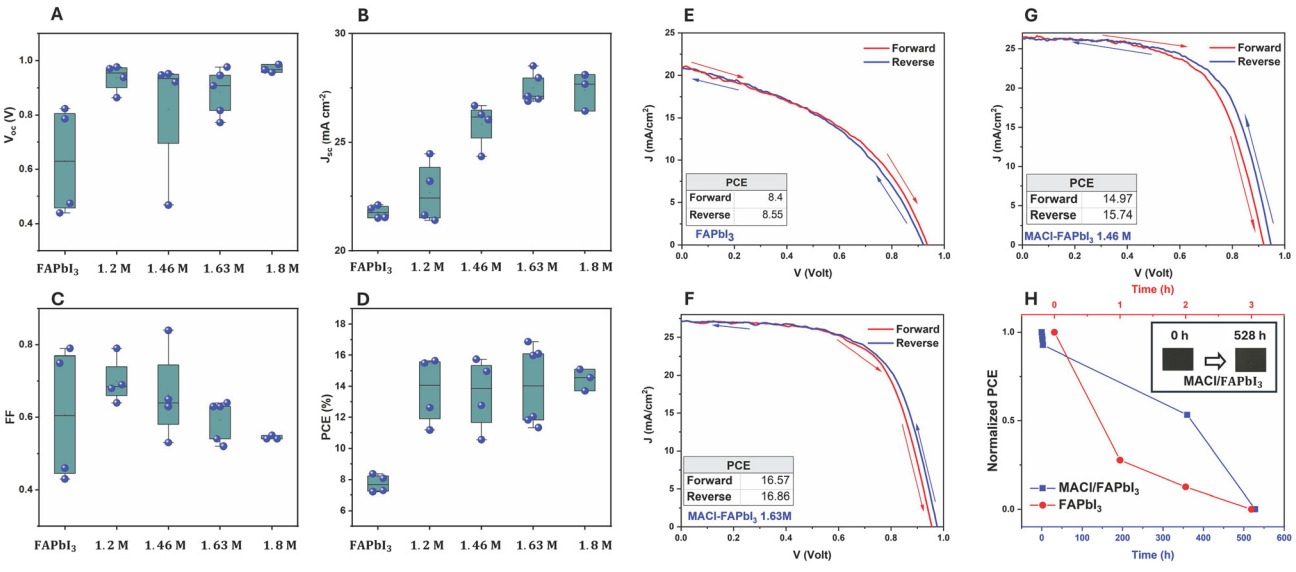

Fig. 7 (A–D) Statistical distributions of photovoltaic parameters (J_{sc}, V_{oc}, FF, and PCE) for MACl-treated FAPbI3 devices fabricated from different precursor formulations. The 1.46 M, 1.63 M, and 1.8 M devices contain 20 mol% MACl, whereas the 1.2 M device uses 50 mol% MACl (chloride-rich condition). (E) Representative forward/backward *J–V* curves for $FAPbI_3$. (F and G) Representative forward/reverse *J–V* curves for the best-performing devices. (H) The long-term stability test of $FAPbI_3$ and $MACl/FAPbI_3$ stored in N_2 for over 500 h without encapsulation.

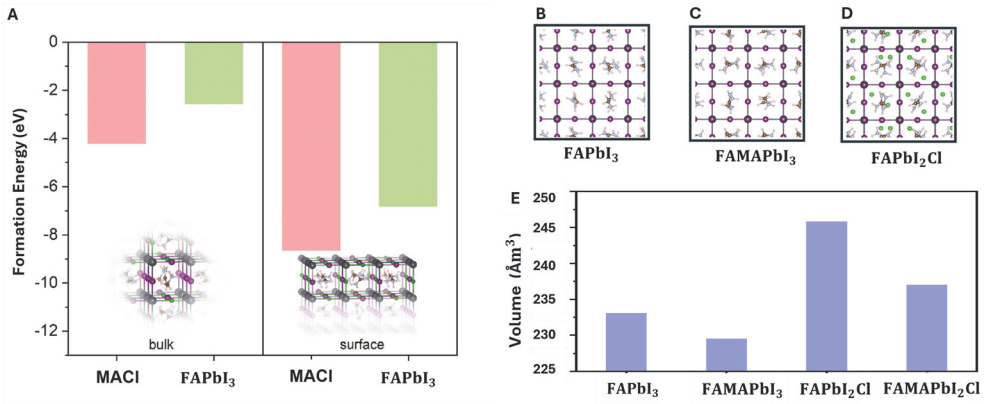

Fig. 8 (A) Formation energy of bulk and surface structures for undoped and MACl-doped $FAPbI_3$. (B) Pristine perovskite structure, (C) perovskite structure with added MA^+, (D) perovskite structure with added Cl^-, and (E) volume values compared to the doping case.

ing in higher J_{sc} and ultimately better device efficiency, despite a modest reduction in FF. Improved charge-carrier collection is supported by the reduced Stokes shift, comparable TRPL lifetimes, improved crystallinity and phase purity, and the enhanced device FF, which together indicate reduced recombination losses and more efficient carrier extraction. Similar behavior has been reported by Joo and Choi, who observed that MACl incorporation enhanced the intensity of the (001) diffraction peak and correlated this structural improvement with increased PCE in $FAPbI_3$-based perovskite solar cells.[24] The effects of MA^+ cations and Cl^- anions incorporated into the perovskite structure were investigated using DFT calculations. The simulated α-$FAPbI_3$ phase exhibits a lower surface energy with MACl at the (001) plane, favoring homogeneous growth and explaining the larger grains observed in SEM (Fig. 2). Incorporation of MA^+ induces a ~1.5% volume contraction, while Cl^- incorporation leads to a ~1.6% expansion; when both ions are present, these effects nearly cancel, resulting in <0.5% net lattice change. This agrees with the experimental XRD data, where no systematic or monotonic peak shift is observed beyond minor lattice adjustments (<2%), and the overall lattice framework remains preserved within the instrumental resolution limit, despite the clear improvement in α-phase purity (Fig. 3). As shown in Fig. 8, the MACl-doped structures also exhibit lower formation energies for both bulk and surface models compared to pristine $FAPbI_3$, indicating greater thermodynamic stability. These quantitative results confirm that MACl incorporation not only stabilizes the α-phase lattice but also correlates with the enhanced crystallinity and phase purity observed experimentally.

Mechanism of MACl-induced crystal growth and phase stabilization

Experimental and computational results clarify how MACl influences the formation and stability of $FAPbI_3$ films. DFT shows that MACl lowers the surface energy of the (001) facet, which can promote oriented growth and improved crystallinity, consistent with SEM and XRD. PL/TRPL measurements indicate that MACl treatment does not markedly alter the intrinsic recombination dynamics (with comparable lifetimes in the representative formulation) while optical signatures such as reduced Stokes shift are consistent with suppressed defect-assisted relaxation. Finally, MA^+-induced slight lattice contraction and Cl^--related lattice expansion compensate each other, resulting in minimal net lattice change and stabilizing the α-phase without a systematic XRD peak shift beyond minor lattice variations. Together, these effects explain the suppression of δ-phase impurities (phase/structural stability), reduced recombination losses (electronic quality), and the improved operational stability evidenced by enhanced PCE retention during aging (Fig. 7H). Notably, the thermodynamic lattice stabilization inferred from DFT and the operational device stability observed experimentally are consistent trends, but they remain conceptually distinct.

Conclusion

This study systematically investigated MACl-assisted $FAPbI_3$ perovskite solar cells by combining a constant-additive molarity series (1.46, 1.63, and 1.8 M with 20 mol% MACl) with a chloride-rich reference formulation (1.2 M with 50 mol% MACl). A key outcome is that MA^+ and a residual amount of Cl^- can remain in the perovskite film after annealing, as supported by XRD/EDS characterization and further rationalized by DFT calculations. MACl treatment enhances α-phase purity and strengthens the (001) preferential orientation, which is associated with reduced grain-boundary losses and more efficient charge extraction, thereby improving the fill factor (FF). In parallel, improved phase quality and suppressed non-radiative recombination contribute to higher V_{oc}, while increased absorption intensity and improved carrier collection lead to enhanced J_{sc}. Across the constant MACl series, optimized precursor molarity (1.63–1.8 M) maximizes current generation and overall efficiency. DFT calculations further show that MA^+-induced lattice contraction and Cl^--induced

expansion compensate each other, yielding minimal net lattice change and stabilizing the α-$FAPbI_3$ framework. Importantly, this compensation explains why chloride retention may not produce a clear lattice-parameter signature in XRD and can therefore be difficult to unambiguously identify experimentally. Overall, by decoupling precursor molarity from additive loading and establishing a clear structure–property–device correlation, this work provides a more systematic and mechanistic understanding of MACl-assisted stabilization in FA-based perovskites and offers practical guidance for processing optimization.

Author contributions

MA, CD, NSS designed and supervised the research. NSS, PK, AC, IT, NG, KE, EC, MA performed the synthesis, film fabrication, device measurements and all film characterizations. IY, CD, NSS performed the DFT computations and materials screening calculations. MA, CD, and NSS wrote the first draft of the manuscript, and all authors contributed feedback and comments.

Conflicts of interest

There are no conflicts to declare.

Data availability

The data supporting this article are included as part of the supplementary information (SI). Supplementary information is available. See DOI: https://doi.org/10.1039/d5dt03070f.

Acknowledgements

This work was financially supported by The Scientific and Technological Research Council of Turkiye (TUBITAK) under award number 121F384 (Awarded to Mustafa Alevli). Computing resources used in this work were provided by the National Center for High-Performance Computing of Turkey (UHEM) under grant number 1015902023.

References

1 J. H. Heo, D. H. Song and S. H. Im, *Adv. Mater.*, 2014, **26**, 8179–8183.
2 N. Pellet, P. Gao, G. Gregori, T. Y. Yang, M. K. Nazeeruddin, J. Maier and M. Grätzel, *Angew. Chem., Int. Ed.*, 2014, **53**, 3151–3157.
3 K. Zhang, B. Ding, C. Wang, P. Shi, X. Zhang, C. Liu, Y. Yang, X. Gao, R. Wang and L. Tao, *Nano-Micro Lett.*, 2023, **15**, 138.
4 H. Min, M. Kim, S.-U. Lee, H. Kim, G. Kim, K. Choi, J. H. Lee and S. I. Seok, *Science*, 2019, **366**, 749–753.
5 Y. Wang, X. Liu, T. Zhang, X. Wang, M. Kan, J. Shi and Y. Zhao, *Angew. Chem.*, 2019, **131**, 16844–16849.
6 C. Mu, J. Pan, S. Feng, Q. Li and D. Xu, *Adv. Energy Mater.*, 2017, **7**, 1601297.
7 M. Kim, G.-H. Kim, T. K. Lee, I. W. Choi, H. W. Choi, Y. Jo, Y. J. Yoon, J. W. Kim, J. Lee and D. Huh, *Joule*, 2019, **3**, 2179–2192.
8 J. Qing, X. K. Liu, M. Li, F. Liu, Z. Yuan, E. Tiukalova, Z. Yan, M. Duchamp, S. Chen and Y. Wang, *Adv. Energy Mater.*, 2018, **8**, 1800185.
9 J. Park, J. Kim, H.-S. Yun, M. J. Paik, E. Noh, H. J. Mun, M. G. Kim, T. J. Shin and S. I. Seok, *Nature*, 2023, **616**, 724–730.
10 C. Wang, B. He, M. Fu, Z. Su, L. Zhang, J. Zhang, B. Mei and X. Gao, *Crystals*, 2024, **14**, 399.
11 S. Liu, J. Li, W. Xiao, R. Chen, Z. Sun, Y. Zhang, X. Lei, S. Hu, M. Kober-Czerny and J. Wang, *Nature*, 2024, **632**, 536–542.
12 B. Conings, J. Drijkoningen, N. Gauquelin, A. Babayigit, J. D'Haen, L. D'Olieslaeger, A. Ethirajan, J. Verbeeck, J. Manca and E. Mosconi, *Adv. Energy Mater.*, 2015, **5**, 1500477.
13 D.-H. Kang, S.-U. Lee and N.-G. Park, *ACS Energy Lett.*, 2023, **8**, 2122–2129.
14 G. S. Shin, S. G. Kim, Y. Zhang and N. G. Park, *Small Methods*, 2020, **4**, 1900398.
15 G. S. Shin, Y. Zhang and N.-G. Park, *ACS Appl. Mater. Interfaces*, 2020, **12**, 15167–15174.
16 J. P. Perdew, A. Ruzsinszky, G. I. Csonka, O. A. Vydrov, G. E. Scuseria, L. A. Constantin, X. Zhou and K. Burke, *Phys. Rev. Lett.*, 2008, **100**, 136406.
17 G. Kresse and J. Furthmüller, *Comput. Mater. Sci.*, 1996, **6**, 15–50.
18 J. P. Perdew, K. Burke and M. Ernzerhof, *Phys. Rev. Lett.*, 1996, **77**, 3865.
19 Q. Li, Y. Xiang, R. Zheng, C. Li, K. Ren, B. Yao, H. Xu, S. Liu, Y. Tan and Z. Fang, *Energy Fuels*, 2022, **37**, 791–797.
20 J. Ruellou, M. Courty and F. Sauvage, *Adv. Funct. Mater.*, 2023, **33**, 2300811.
21 A. Jana, Q. Ba, A. S. Nissimagoudar and K. S. Kim, *J. Mater. Chem. A*, 2019, **7**, 25785–25790.
22 H. B. Lee, M. K. Jeon, N. Kumar, B. Tyagi and J. W. Kang, *Adv. Funct. Mater.*, 2019, **29**, 1903213.
23 S. Gull, M. H. Jamil, X. Zhang, H. s. Kwok and G. Li, *ChemistryOpen*, 2022, **11**, e202100285.
24 S. H. Joo and H. W. Choi, *Coatings*, 2021, **11**, 1184.

